Electrochemical and Spectroscopic Study of Mononuclear Ruthenium Water Oxidation Catalysts: A Combined Experimental and Theoretical Investigation

J.M. de Ruiter[a], R.L. Purchase[a], A. Monti[a], C.J.M. van der Ham[a], M. P. Gullo[c], K.S. Joya[a,b], M. D'Angelantonio[c], A. Barbieri[c], D.G.H Hetterscheid[a], H.J.M. de Groot[a], F. Buda[a]

[a] Leiden University, Leiden Institute of Chemistry, Einsteinweg 55, 2300 RA, Leiden, The Netherlands

[b] Division of Physical Sciences and Engineering, KAUST Catalysis Center (KCC), King Abdullah University of Science and Technology (KAUST), 4700 KAUST, Thuwal 23955-6900, Saudi Arabia

[c] ISOF-CNR Area della Ricerca di Bologna, Via Pietro Gobetti 101, 40129 Bologna, Italy

Abstract

One of the key challenges in designing light-driven artificial photosynthesis devices is the optimisation of the catalytic water oxidation process. For this optimisation it is crucial to establish the catalytic mechanism and the intermediates of the catalytic cycle, yet a full description is often difficult to obtain using only experimental data. Here we consider a series of mononuclear ruthenium water oxidation catalysts of the form $[Ru(cy)(L)(H_2O)]^{2+}$ (cy = *p*-cymene, L = 2,2'-bipyridine and its derivatives). The proposed catalytic cycle and intermediates are examined using density functional theory (DFT), radiation chemistry, spectroscopic techniques and electrochemistry to establish the water oxidation mechanism. The stability of the catalyst is investigated using Online Electrochemical Mass Spectrometry (OLEMS). The comparison between the calculated absorption spectra of the proposed intermediates with experimental ones, as well as free-energy calculations with electrochemical data, provides strong evidence for the proposed pathway: a water oxidation catalytic cycle involving four proton-coupled electron transfer (PCET) steps. The thermodynamic bottleneck is identified in the third PCET step involving the O-O bond formation. The good agreement between the optical and thermodynamic data with DFT predictions further confirms the general applicability of this methodology as a powerful tool in the characterisation of water oxidation catalysts and for the interpretation of experimental observables.

Introduction

In recent years, an increasing amount of attention has been invested in the search for abundant renewable energy sources. Although solar energy is one of the largest useful renewable energy sources,[1] it is intermittent and diffuse. One promising method of harnessing the potential of this energy source is the conversion of sunlight directly into fuels such as H_2 by means of artificial photosynthesis.[2,3] However, devising a cost effective and practical way of doing so remains a significant challenge. Water oxidation catalysts (WOCs) are a key component of the artificial photosynthetic system.[4–14] Initially, it was supposed that only multinuclear complexes would be able to supply the oxidation potential needed to catalyse water splitting, in analogy with the four Mn complex in the oxygen evolving centre of Photosystem II.[8,15] As a result, several molecular catalysts have been developed with two or more metal sites.[2,8,11,16–19] Recently, a shift of attention has occurred, directing more effort towards developing mononuclear WOCs.[8,20] A large number of ruthenium[4–9,13,21–23] and iridium[8,11,14,24–29] based catalysts have been reported. Density Functional Theory (DFT) has been used extensively to predict the reaction mechanisms and the electronic properties of several multi- and mono-nuclear molecular catalysts.[4,11,13,18,22,29]

A full description of the mechanisms underlying catalytic activity is not always accessible experimentally. Therefore, a computational description of each intermediate state plays a crucial role in the prediction of catalytic behaviour throughout the entire cycle and provides complementary information for the interpretation of experimental observations. Concurrently, the computational approach also needs to be validated with experimental data.

We recently investigated the WOC $[Ru(cy)(bpy)(H_2O)]^{2+}$ (cy = *p*-cymene, bpy = 2,2'-bipyridine; Scheme 1 (*Ru*-bpy)).[21,30] It has been shown that the immobilization of this Ru-based catalyst, modified with surface anchoring units, on a $BiVO_4$ light-absorber enhances the performance of this photoanode.[30] The proposed catalytic cycle for water oxidation involves four proton-coupled electron transfer (PCET) steps as depicted in Scheme 1.[31]

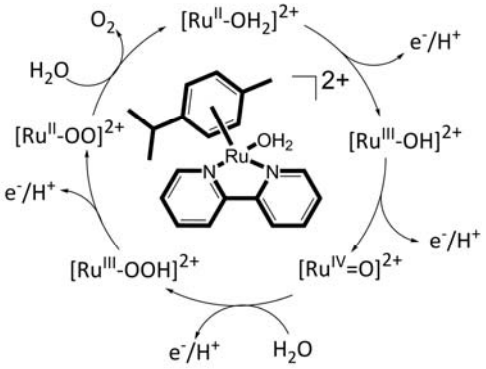

Scheme 1. Proposed catalytic cycle for water oxidation by *Ru*-bpy. Inset: Schematic structure of *Ru*-bpy.

Here we study this *Ru*-bpy catalyst and several derivative catalysts of the form $[Ru(cy)(L)(H_2O)]^{2+}$ (Figure 1) by means of a combination of theoretical and experimental techniques, expanding on previously described strategies.[13] We verify the stability of this class of catalysts under oxidative conditions using Online Electrochemical Mass Spectrometry (OLEMS) and Surface Enhanced Raman Spectroscopy (SERS).[32] The proposed catalytic mechanism is validated by comparing the computed free-energy differences between the intermediates in the catalytic cycle and those derived from

electrochemical measurements. The absorption spectra predicted by time-dependent DFT (TDDFT) calculations for each intermediate in the catalytic cycle are used to interpret the results obtained from stopped-flow and pulse radiolysis measurements, confirming that the proposed cycle can explain experimental observation. Finally, the ability of TDDFT calculations to reproduce absorption spectra for three derivative catalysts confirms the general applicability of this methodology as a powerful tool for the characterisation of WOCs and for the interpretation of experimental observables.

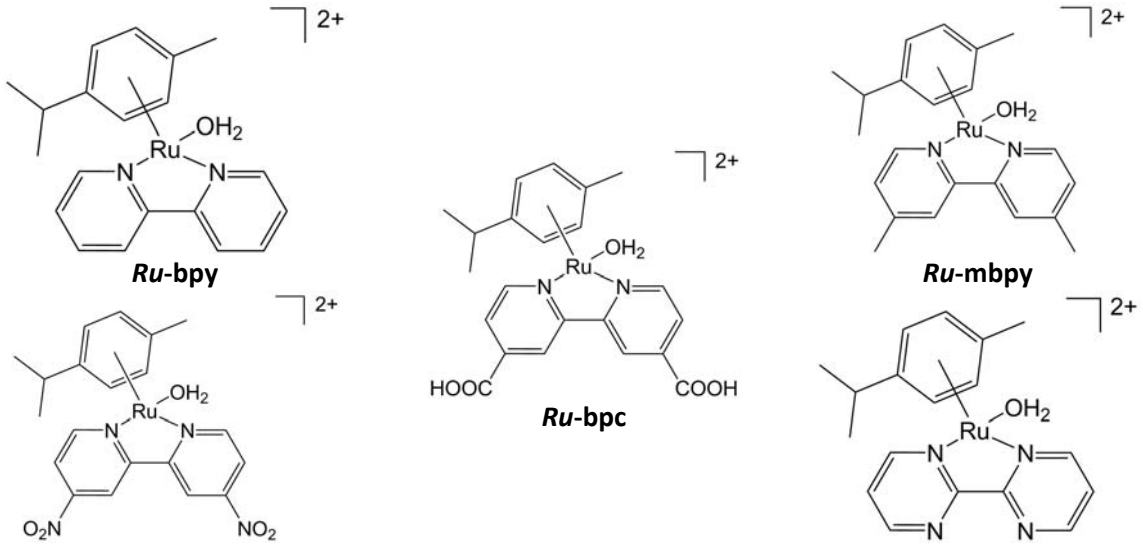

Figure 1. Schematic structures of the investigated catalysts: 2,2′-bipyridine (*Ru*-bpy), 4,4′-disubstituted-2,2′-bipyridine (*Ru*-bpc, *Ru*-mbpy, *Ru*-dnbpy) and 2,2′-bipyrimidine (*Ru*-bpm) Ru(*p*-cymene) complexes.

Experimental section

The synthesis of the starting compounds is outlined in the Supporting Information and summarised in Table S1. Proton NMR spectra were obtained with a Bruker WM-300 MHz spectrophotometer and are also shown in the SI.

Cyclic voltammetry

Cyclic voltammetry measurements were carried out in a three-electrode configuration double junction H-type Pyrex glass cell. The working electrode was an ITO-coated glass slide (Aldrich 2.5 cm x 2.5 cm, 8-12 Ω/sq). A platinum wire (thickness 1 mm) shaped into a spiral, was used as a counter electrode. A silver-silver chloride electrode was used as a reference electrode. The ITO-coated glass slides were cut in half and cleaned by sonication in methanol. A little less than half the cleaned slide was dipped in the solution to yield a working electrode area of ~1 cm^2. The platinum counter electrode was cleaned by soaking in 6 M H_2SO_4 overnight. pH 1 measurements were made in 0.1 M HNO_3. pH 7 measurements were made in 0.1 M phosphate buffer (obtained from Aldrich). In both cases, *Ru*-bpc was dissolved in the solution at a concentration of 1 mM. Experiments were performed with an Autolab Metrohm potentiostat controlled by GPES v.4.9 software.

Online Electrochemical Mass Spectrometry (OLEMS)

OLEMS experiments were performed using a set up that has been previously described.[32,33] The electrochemical cell used for these experiments is a two compartment cell with three electrodes: a gold bead electrode (diameter 3 mm) and a gold wire were used as the working and counter electrodes, respectively; the reference electrode was an RHE separated from the main cell by a Luggin capillary. Before each measurement, the working electrode was electrochemically cleaned: the electrode was first oxidized in 10% sulfuric acid by applying 10 V for 30 s, using a graphite bar as the counter electrode. Subsequently the gold oxide formed was removed by dipping the working electrode in a 6 M HCl solution for 30 s. The electrode was then flame annealed and cycled 200 times from 0 – 1.75 V (vs. RHE) at 1 V/s in 0.1 M $HClO_4$. The gold counter electrode was flame annealed. A 0.1 M solution of phosphate buffer (pH 7) was prepared from Na_2HPO_4 and NaH_2PO_4. *Ru*-bpc was dissolved in the buffer solution at a concentration of 1 mM and OLEMS measurements were made with the catalyst in solution.

Surface Enhanced Raman Spectroscopy

In situ Surface Enhanced Raman Spectroscopy (SERS) electrochemistry was performed on a set up that has been previously described.[32,34,35] The electrochemical cell has two compartments and three electrodes: a roughened gold surface as the working electrode, a gold wire as the counter electrode, and the reference electrode was an RHE separated from the main cell by a Luggin capillary. The gold working electrode was first electrochemically cleaned using the process described above for the OLEMS measurements and then subsequently electrochemically roughened by 25 oxidation−reduction cycles (ORC) in a 0.1 M solution of KCl. The ORC were performed between −0.30 and 1.20 V vs SCE, during which the potential was held for 30 s at the negative limit and for 1.3 s at the positive limit, a method reported to give a brownish surface that is SERS active.[36] 1 mg *Ru*-bpc was dissolved in methanol. A neutral Na-exchanged Nafion solution was prepared by mixing one part of Nafion (5% wt, 1000 equiv/g, Sigma-Aldrich) with one part of 0.05 M NaOH.[37] One part of the catalyst solution was mixed with one part of Na-exchanged Nafion solution. 15 µL of this mixture

was dropcast on the gold working electrode and dried under vacuum for use in the in situ SERS electrochemical measurements.

UV-Vis Spectroscopy and Stopped Flow analysis

Absorption spectra of the $[Ru(cy)(L)(H_2O)]^{2+}$ complexes (c = 5×10^{-5} M) for both molar absorptivity measurements and kinetic analysis were recorded with a Perkin-Elmer Lambda 950 UV/Vis/NIR spectrophotometer. The kinetic analysis was performed using an Applied Photophysics stopped-flow system configured for two-syringe mixing (RX.2000 Stopped-Flow Mixing Accessory). The initial concentrations of reactants in the syringes were fixed to 10^{-4} M for Ru(II) complexes in every experiment and from 1×10^{-4} M to 10×10^{-4} M for Ce^{IV} ($[Ce(NH_4)_2(NO_3)_6]$, CAN, Sigma-Aldrich), depending on the different Ru/Ce ratio (1:1; 1:2; 1:4 and 1:10). The spectral evolution was recorded after equal amounts of both solutions were mixed in a 1 cm optical path length stopped-flow cell. The dead time of the mixing setup was 8 ms.

Pulse radiolysis

Pulse radiolysis[38] with optical absorption detection was performed using a 12 MeV linear accelerator, which delivered 100 - 200 ns electron pulses with doses between 4 and 82 Gy.[39] The pulse irradiations were performed at room temperature (22 ± 2 °C) on samples in Spectrosil quartz cells of 2 cm optical path length. Solutions were protected from the analysing light with a shutter and cut-off filters. The bandwidth used throughout the pulse radiolysis experiments was 5 nm. The radiation dose per pulse was monitored with a charge collector placed behind the irradiation cell and calibrated with an N_2O-saturated solution containing 0.1 M HCO_2^- and 0.5 mM methylviologen ($MV^{+\bullet}$), using $G(MV^{+\bullet}) = 0.7\times10^{-6}$ mol J^{-1} at 605 nm, where $G(x)$ represents the number of moles of species x formed, consumed or altered per joule of energy absorbed by the system.[40]

The radiolysis of water yields solvated electrons (e_{aq}^-), hydroxyl radicals ($^\bullet OH$) and hydrogen atoms ($H^\bullet$) as primary radical species, which are responsible for the production of the several active species in solution.[41] The oxidants used in the experiments here were $SO_4^{\bullet-}$ and $CO_3^{\bullet-}$. They were chosen for their high standard redox potentials of 2.43 and 1.5 V (vs. NHE), respectively.[42–44] $SO_4^{\bullet-}$ radicals were generated by pulse radiolysis of a $K_2S_2O_8$ (10 mM) solution de-aerated with Argon, at pH=1.4 adjusted by adding concentrated $HClO_4$, in the presence of 0.1 M *t*-BuOH as $^\bullet OH$ radical scavenger. $CO_3^{\bullet-}$ radicals were generated by pulse radiolysis of Na_2CO_3 / $NaHCO_3$ (5 mM : 5mM, pH = 10) solution saturated with N_2O. The mechanisms for the production of the radicals is described in reference [44].

Computational method and details

Geometry optimisations, thermodynamic and TDDFT calculations are performed using the Amsterdam Density Functional (ADF) software package.[45–47] Van der Waals interactions are accounted for by using the Grimme3 BJDAMP dispersion correction.[48] Unless stated otherwise the geometries of the examined molecules are optimised using the OPBE functional,[49] with the TZP (triple zeta polarized) basis set and a small core. This GGA functional has shown good performance when describing transition metal complexes. [21,50–52] Time dependent density functional theory (TDDFT) excited state calculations are performed with the B3LYP functional combined with the TZP basis set.[53] In both the geometry optimization and the TDDFT calculations, the solvation effect of water is included by means of the conductor-like screening model COSMO.[54] All calculations are spin unrestricted and the energetically most stable multiplicity is checked when necessary (see Table S2).

This computational set-up is employed in test calculations performed on a ruthenium-based benchmark WOC, for which experimental data is available for comparison.[13] The results shown in the Supporting Information (Figure S1 and Table S3) validate the ability of this method to accurately reproduce the optical properties of compounds chemically similar to the WOC of interest in this study.

The thermodynamics of the catalytic cycle is obtained by calculating the Gibbs free energy difference between each catalytic intermediate following the method first proposed by Norskov and co-workers.[55–57] The structure of each intermediate is optimised at the B3LYP/TZP level, in vacuum. Zero-point energy and entropic contributions are included through vibrational analysis performed with the same computational set-up. For every structure optimised in vacuum, solvation effects are accounted for by performing a single point calculation with the B3LYP functional in a water environment simulated with the COSMO model. Reaction energies, zero-point energies and entropies of O_2, H_2 and H_2O are also calculated in this manner. Furthermore, as the catalytic cycle proceeds via PCET, the free energy of the proton and electron are calculated as a pair: $H^+ + e^- \rightarrow ½\ H_2$.

Raman frequency calculations, after re-optimisation of the geometries, are performed with Gaussian '09,[58] using the B3LYP functional and LANL2DZ basis set.[59–61] In Gaussian '09 calculations, this basis set has been shown to be an effective descriptor for ruthenium complexes.[62,63]. Solvation effects are included with the IEF-PCM model for water,[64] while anharmonic corrections were not included. The resulting output is visualised with the help of the GaussSum program.[65]

Results and Discussion

Characterisation of the catalytic intermediates of *Ru*-bpc

Catalyst stability

The stability of similar WOC complexes under oxidative conditions has been under scrutiny in the literature due to the possible oxidative degradation and loss of the ligands.[66,67] In particular, evidence of catalyst degradation has been reported for Ir-Cp* complexes (Cp* = cyclopentandienyl). [66,67] These results appear to be strongly affected by the chemical oxidant used in the study, most often Cerium Ammonium Nitrate (CAN) or Sodium Periodate $NaIO_4$.[66–77] More recently it has been shown that the Cp* complex remains intact at the initial stages of the water oxidation reaction in the case of $[Ir(Cp^*)(Me_2NHC)(Cl)_2]$.[32]

To establish the stability of the Ru-based catalysts analysed in this work, we use OLEMS monitoring *in situ* the production of O_2 and CO_2 concurrently with time dependent electrolysis.[32] In this way it is possible to check whether the organic moieties in the complex decompose during catalytic oxygen evolution. Figure 2 shows the current signal and the mass signals for O_2 (m/z 32) and CO_2 (m/z 44).

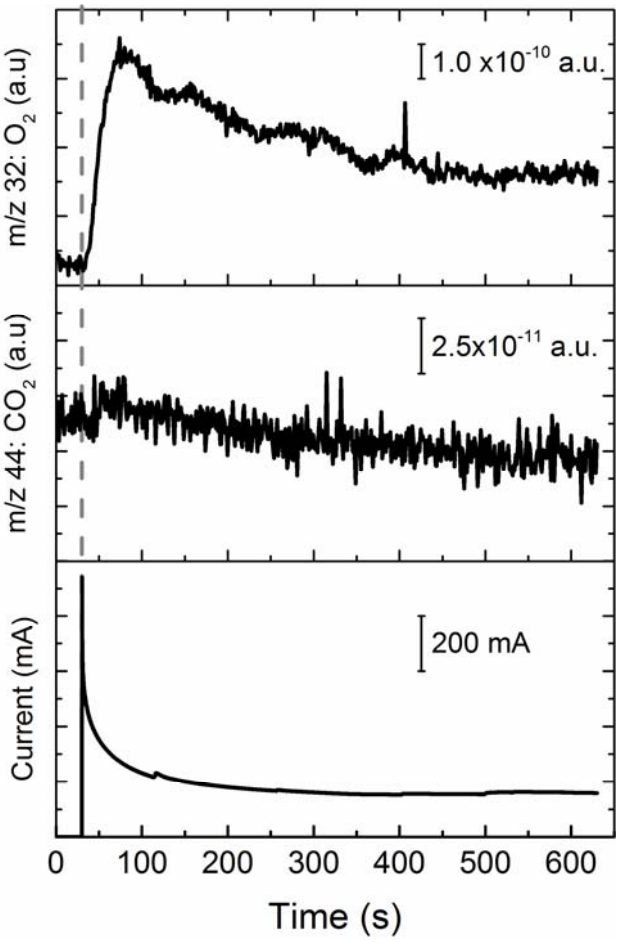

Figure 2. OLEMS signals acquired during electrochemical water oxidation as catalysed by *Ru*-bpc. The potential is initially set at 0.8 V (vs NHE) then increased to 1.8 V at 30 s (indicated by the dashed grey line).

Figure 2 shows that when the potential is raised to a value above 0.8 V where water oxidation begins (see also Table 1), then there is a marked increase in current and oxygen is evolved. In contrast, there is little change in the CO_2 signal. These results show that *Ru*-bpc forms negligible amounts of carbon dioxide under oxidizing conditions, strongly suggesting that the organic ligands are stable, or at least do not degradate all the way to CO_2. The instantaneous evolution of dioxygen as soon as a sufficiently high potential is applied, illustrates that *Ru*-bpc itself is the active species in the oxygen evolution reaction at early stages of the water oxidation reaction.[78] We cannot rule out that the cymene ligand de-coordinates after prolonged electrolysis under the harsh oxidative conditions and the decrease in oxygen evolution rates after the initial burst may actually point to such an event. Since we do not detect significant amounts of CO_2 under these circumstances, this indicates that *Ru*-bpc does not degradate all the way to ruthenium oxide under the employed conditions. This is also consistent with our previous investigation involving the use of highly sensitive in-situ electrochemical quartz crystal nanobalance (EQCN) experiments showing no sign of ruthenium oxide generation during the catalytic reaction of water oxidation.[30]

Electrochemical and Thermodynamic investigation

Electrochemical investigations and cyclic voltammetry (CV) has been performed for the *Ru*-bpc and *Ru*-bpy complexes. To assign a specific redox couple to each electronic wave observed in the CV analyses (shown in Figures S2 – S4), we compute with DFT the Gibbs free energy differences between consecutive catalytic intermediates according to the proposed cycle presented in Scheme 1. As shown in Table 1 and Figure 3. the theoretical calculations show good agreement with the experimentally observed trend. Consistent with the experimental data, the third step from $[Ru^{IV}=O]^{2+}$ to $[Ru^{III}\text{-}OOH]^{2+}$ (which involves the formation of the O-O bond) shows the largest ΔG, and thereby forms the thermodynamic bottleneck of the system. This thermodynamic bottleneck gives an overpotential of about 0.6 V for both *Ru*-bpc and *Ru*-bpy, as estimated from the electrochemical data (see Table 1). As the $[Ru^{II}\text{-}OO]^{2+}$ intermediate cannot be observed experimentally, it is not possible to comment on the redox value calculated for it. It is interesting to note that the DFT results predict the final step involving the ligand exchange of O_2 with H_2O on the Ru site to be thermodynamically spontaneous with a ΔG= -0.42 eV for *Ru*-bpc and ΔG= -0.15 eV for *Ru*-bpy, contrary to the general assumption that this exchange is thermodynamically neutral.[57]

The comparison of the thermodynamic analysis of the two catalysts *Ru*-bpc and *Ru*-bpy (see Table 1) shows that the substitution of a COOH group for H seems to have little effect on the potentials at which the PCET steps occur. The two catalysts only differ by around 0.1 eV when comparing the measured ΔG values for each catalytic step. We do notice however that the DFT method used seems to over-stabilise the initial state of *Ru*-bpc leading to a deviation of 0.45 eV for the $[Ru^{II}\text{-}OH_2]^{2+} \rightarrow [Ru^{III}\text{-}OH]^{2+}$ step. This is also reflected in the ΔG values calculated for the final ligand exchange mentioned earlier: that calculated for *Ru*-bpc is 0.3 eV more negative than that calculated for *Ru*-bpy. It is noted that the initial state has also been shown to be the most dependent on the choice of functional.[79] Apart from the steps affected by the over-stabilisation of the initial state of *Ru*-bpc, the calculated ΔG values for both catalysts differ less than 0.1 eV. The $[Ru^{III}\text{-}OH]^{2+} \rightarrow [Ru^{IV}=O]^{2+}$ step as calculated for *Ru*-bpc agrees to 0.1 eV with the experimental measurement, while a larger deviation (0.2 eV) is observed for the $[Ru^{IV}=O]^{2+} \rightarrow [Ru^{III}\text{-}OOH]^{2+}$ step. This step has the largest deviation between calculated and experimental values for the *Ru*-bpy catalyst, while the experimental values for the first two catalytic steps are reproduced with an error ≤ 0.2 eV.

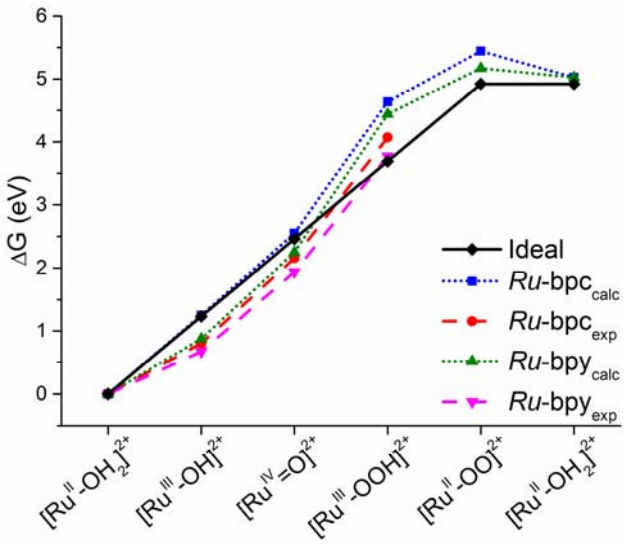

Figure 3. Free energy difference between intermediates along the catalytic pathway of the *Ru*-bpy catalyst. DFT results (red) are compared with the values extracted from electrochemical data (blue). We also show for comparison the optimal catalyst case (black) corresponding to a change in free energy of 1.23 eV for all four steps.

Table 1 Calculated ΔG for each catalytic step along the proposed catalytic mechanism, as compared to the experimentally measured ΔG for *Ru*-bpc and *Ru*-bpy adjusted to pH 0 according to the Nernst equation.

	ΔG_{calc} *Ru*-bpc (eV)	ΔG_{exp} *Ru*-bpc (eV)	ΔG_{calc} *Ru*-bpy (eV)	ΔG_{exp} *Ru*-bpy (eV)
$[Ru^{II}\text{-}OH_2]^{2+} \rightarrow [Ru^{III}\text{-}OH]^{2+}$	1.25	0.80	0.87	0.67
$[Ru^{III}\text{-}OH]^{2+} \rightarrow [Ru^{IV}\text{=}O]^{2+}$	1.30	1.36	1.38	1.27
$[Ru^{IV}\text{=}O]^{2+} \rightarrow [Ru^{III}\text{-}OOH]^{2+}$	2.09	1.91	2.19	1.83
$[Ru^{III}\text{-}OOH]^{2+} \rightarrow [Ru^{II}\text{-}OO]^{2+}$	0.81	-	0.73	-
$[Ru^{II}\text{-}OO]^{2+} \rightarrow [Ru^{II}\text{-}OH_2]^{2+}$	-0.42	-	-0.15	-
$2H_2O \rightarrow 2H_2 + O_2$	5.02	4.92	5.02	4.92

In Table 1 we also note the computed ΔG associated to the hydrolysis process; this corresponds to the sum of all the ΔG contributions in the complete catalytic cycle. This result deviates only by 0.1 eV with respect to the experimental value of 4.92 eV, thereby providing a further indication that the chosen computational method and set-up is sufficiently accurate in its description of the water oxidation reaction.

SERS and Raman frequency calculations

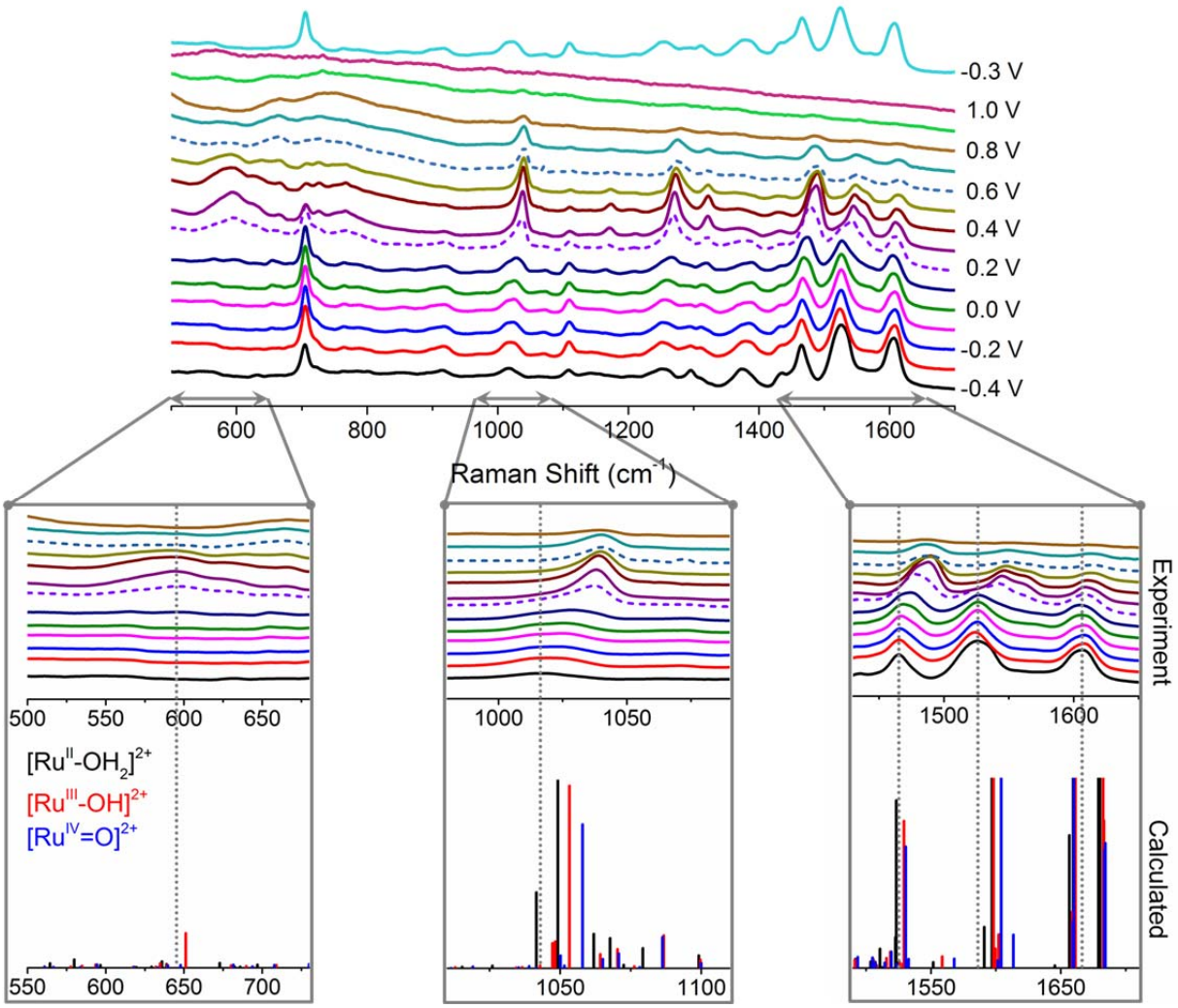

Figure 4. (Top) SERS spectra of *Ru*-bpc. Spectra are obtained by increasing the potential stepwise to 1.0 V, after which a measurement is performed at -0.3 V. The dotted lines indicate the potential at which significant changes are observed. (Bottom panels) Selected regions of SERS spectra of *Ru*-bpc are compared to computed Raman frequencies and intensities for the three intermediates $[Ru^{II}\text{-}OH_2]^{2+}$ (black), $[Ru^{III}\text{-}OH]^{2+}$ (red) and $[Ru^{IV}\text{=}O]^{2+}$ (blue). The grey dotted lines indicate areas in which changes in the Raman spectrum can be linked to different intermediates.

To verify the presence of the expected catalytic intermediates, SERS measurements were conducted stepwise from -0.4 V up to 1.0 V. Owing to the oxidation of the gold electrode, it was not possible to measure SERS spectra at the potentials needed to drive the catalyst through the bottleneck of the third PCET step. After measuring up to 1.0 V, another spectrum was measured at -0.3 V that shows recovery of the initial species. This further indicates that the catalyst remains intact during the initial stages of the water oxidation reaction.

When considering the SERS spectra (Figure 4) three distinct potential ranges (-0.4 – 0.1 V, 0.2 – 0.5 V, 0.6 – 1.0 V) can be identified. The potentials at which these ranges change (0.2 and 0.6 V) are the same as the potentials assigned to the transition from one catalytic intermediate to the next (adjusted for pH 7.35). Considering the potential range for which SERS is conducted, it is expected that only the $[Ru^{II}\text{-}OH_2]^{2+}$, $[Ru^{III}\text{-}OH]^{2+}$ and $[Ru^{IV}\text{=}O]^{2+}$ species will be identifiable. Raman

frequency spectra calculated using Gaussian '09 for these three species are compared to three different selected frequency regions of the SERS spectra in the lower panels of Figure 4.

In the region 500 – 680 cm^{-1}, a broad shoulder appears at 0.2 V, then decays above 0.6 V. In this region, the theoretical spectra shows only one mode attributed to the Ru-OH stretch of the $[Ru^{III}\text{-}OH]^{2+}$ species. The Ru-O stretch of the $[Ru^{II}\text{-}OH_2]^{2+}$ species is expected at lower frequencies and as such is not observed experimentally, while the stiffer Ru=O stretch is expected around 830 cm^{-1}. In the 1010 – 1110 cm^{-1} region, a peak is observed around 1015 cm^{-1} at -0.4 V, which shifts to higher frequency at 0.2 V, then slowly decays and shifts to slightly higher frequencies. Based on the DFT calculations, this peak is assigned to the Ru-N stretch, which becomes stiffer as the oxidation state of the Ru increases. This trend is also shown in the theoretical calculations (see lower panels of Figure 4).

The effect of the increasing oxidation state of Ru on the bonds to the bipyridine ligand is also seen in the region between 1430 and 1670 cm^{-1}. The predicted frequencies are ≈5% higher than the measured values, which is within a typical error at the DFT/B3LYP level of theory. Nevertheless, the trends between calculation and experiment are definitely comparable. Calculation identifies the peak around 1475 cm^{-1} as being due to the carbon-carbon stretch bridging the two pyridines. This mode is therefore more influenced by the changing Ru oxidation state than the other bipyridine hydrogen wags which are calculated at around 1600 cm^{-1}. This is demonstrated in the larger shift towards a stiffer mode as the oxidation state increases for the 1475 cm^{-1} peak. Experiment and calculation show good agreement in this trend. Comparing the calculated Raman modes of *Ru*-bpc to *Ru*-bpy (see Figure S5) one can notice that the COOH groups lead to a number of additional bipyridine modes, due to the additional symmetric and asymmetric stretches possible in the COOH group.

Calculation also correctly predicts the appearance of a shoulder at increasing potentials for the peak observed at 1525 cm^{-1}. This shoulder is due to stiffer cymene modes resulting from stronger coordination to Ru as the catalyst proceeds through the initial steps of the catalytic cycle and Ru becomes more positive. Thus, by comparing SERS measurements and Raman frequency calculations the presence of the proposed early catalytic intermediates is further established.[68,80]

Optical absorption and TDDFT calculations

Further investigation of the expected catalytic intermediates is conducted by comparing experimental absorption spectra with TDDFT calculations for the singly- and doubly-oxidized forms proposed for *Ru*-bpc. The absorption of a *Ru*-bpc solution to which an excess of the oxidant cerium ammonium nitrate (CAN) is added (Ru/Ce ratio = 1:10) is measured over time. After 24 hours two peaks not seen before the introduction of the oxidant were observed. It is noteworthy that the addition of a more moderate excess of CAN (Ru/Ce ratio = 1:4) produced absorption spectra with the same shape as those reported for a ratio 1:10. In Figure 5 the experimental spectra are compared to TDDFT B3LYP spectra calculated for $[Ru^{II}\text{-}OH_2]^{2+}$ and the catalytic intermediates, $[Ru^{III}\text{-}OH]^{2+}$ and $[Ru^{IV}\text{=}O]^{2+}$. The peak characteristic of Ce^{IV} (around 320 nm) was also investigated over time in experiments conducted with *Ru*-bpy, decreasing in intensity as shown in Figure S6. Calculated spectra for all the proposed *Ru*-bpy catalytic intermediates are also shown in Figure S7.

The spectrum measured before addition of CAN (Figure 5, solid black line) shows good agreement with the one calculated for the starting species, $[Ru^{II}\text{-}OH_2]^{2+}$ (Figure 5, dotted black line). In both

experimental and calculated spectra a signal peaking around 380 nm and tailing over 450 nm is observed. This band is commonly detected in *arene*-Ru^{II} complexes with one bidentate bipyridyl ligand,[81] and is attributed to a metal-to-ligand charge-transfer (MLCT) transition. The nature of such transition is well described by TDDFT (see Figure S8). The intense band at wavelengths shorter than 350 nm, assigned to a ligand-centred transition,[81] is also well reproduced by B3LYP.

The spectrum measured 24 hours after the introduction of 10 equivalents of CAN (Figure 5, solid red line) can be interpreted by comparison with the TDDFT results obtained for the intermediates $[Ru^{III}\text{-}OH]^{2+}$ (Figure 5, blue dotted line) and $[Ru^{IV}{=}O]^{2+}$ (Figure 5, red dotted line). The best comparison is observed with the spectrum calculated for the catalytic intermediate $[Ru^{IV}{=}O]^{2+}$, obtained after two PCET steps, showing a peak around 530 nm which is associated to a metal centred d-d transition (see Figure S9). This peak is characteristic of the intermediate $[Ru^{IV}{=}O]^{2+}$ and deviates by only ~0.15 eV from the experimental peak observed around 550 nm. This deviation between experiment and theory is within a typical average error for TDDFT calculations using the B3LYP functional. A small shoulder tails off at 600 nm, which can be associated with the tail of the measured spectrum. Furthermore, the energetically higher experimental shoulder observed around 400 – 450 nm matches well with a peak calculated for $[Ru^{IV}{=}O]^{2+}$. It should be noted that although a peak around the same wavelength is also predicted for the intermediate $[Ru^{III}\text{-}OH]^{2+}$, there is no experimental evidence of Ru^{III} formation during chemical oxidation with CAN. This is due to its conversion into a $[Ru^{IV}{=}O]^{2+}$ species at a rate faster than the time resolution of the stopped flow apparatus (t < 2 ms).[13,77]

This analysis suggests that with the excess CAN oxidant used, the catalytic process has stopped after the first two PCET steps at the $[Ru^{IV}{=}O]^{2+}$ intermediate. This result reflects that the third PCET step from $[Ru^{IV}{=}O]^{2+}$ to $[Ru^{III}\text{-}OOH]^{2+}$ requires a driving force larger than the oxidative power of CAN (~ 1.75 eV).[71] Without a stronger applied overpotential, the catalyst will not be able to cross the potential barrier imposed by the formation of the peroxide bond, leaving $[Ru^{IV}{=}O]^{2+}$ as stable final product.

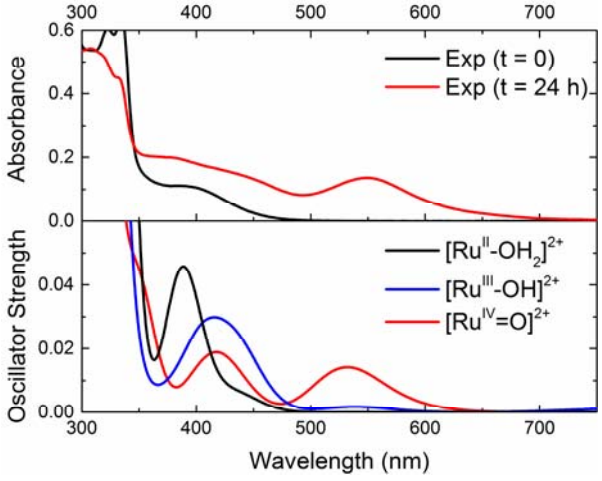

Figure 5. (Top) Experimental absorption spectra of *Ru*-bpc initially in acid (black line) and after 24 hours upon addition of 10 equivalents of CAN (red line). This is compared to the TDDFT spectra (bottom) of $[Ru^{II}\text{-}OH_2]^{2+}$ (black), $[Ru^{III}\text{-}OH]^{2+}$ (blue) and $[Ru^{IV}{=}O]^{2+}$ (red). The calculated spectra have a Gaussian width broadening of 0.3 eV.

Derivative catalysts

The derivative catalysts *Ru*-bpy, *Ru*-mbpy, *Ru*-dnbpy and *Ru*-bpm are also studied using spectroscopic measurements and TDDFT calculations following the same procedure described for the *Ru*-bpc case. The results are shown in Figure 6. Like the spectra discussed earlier for *Ru*-bpc, each of the derivative compounds before addition of 10 eq. CAN (Exp t = 0 in Figure 6) show an intense peak at wavelengths less than 350 nm, accompanied by a less intense peak which appears as a shoulder tailing to 500 nm (see also Table S4 and Figure S10). For *Ru*-bpy and *Ru*-mbpy, a clear peak is also observed around 550 nm 24 hours after addition of CAN (Exp t = 24 h, Figure 6). The computed absorption spectra for the $[Ru^{IV}=O]^{2+}$ intermediate of these two derivatives also show a very good agreement in the position of the peaks seen experimentally after 24 hours. The values computed for the primary excitations of the $[Ru^{IV}=O]^{2+}$ intermediate indicate that the peak arising after 24 hours around 550 nm is characteristic of that specific catalytic state (Table 2). Overall, these results show the importance of TDDFT calculations for the interpretation of the catalytic cycle.

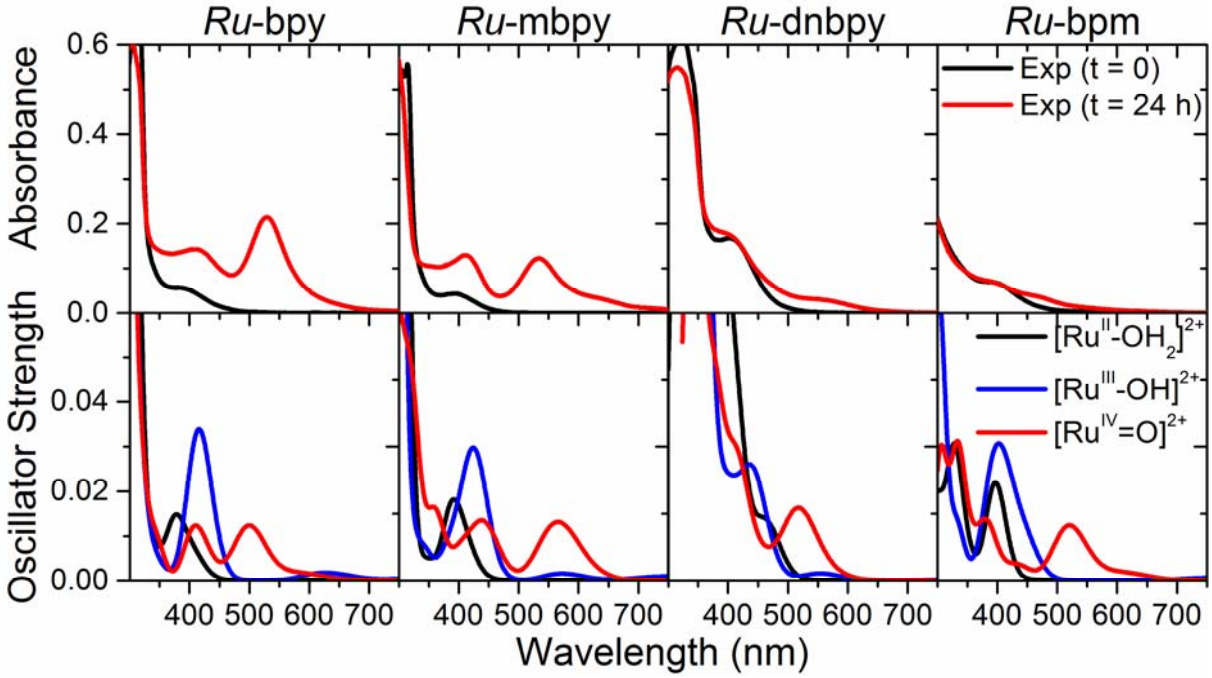

Figure 6. (Top) Experimental absorption spectra of different derivative catalysts initially in acid (black line) and after 24 hours upon addition of 10 equivalents of CAN (red line). This is compared to the TDDFT spectra (bottom) of $[Ru^{II}\text{-}OH_2]^{2+}$ (black), $[Ru^{III}\text{-}OH]^{2+}$ (blue) and $[Ru^{IV}=O]^{2+}$ (red). The calculated spectra have a Gaussian width broadening of 0.3 eV.

Table 2. Primary excitations for the $[Ru^{IV}=O]^{2+}$ intermediates of the examined catalysts calculated using TDDFT, as compared to experiment

		***Ru*-bpc**	***Ru*-bpy**	***Ru*-mbpy**	***Ru*-dnbpy**
Wavelength (nm)	Exp	550	529	534	~ 560
	Calc	530	501	565	519
Energy (eV)	Exp	2.25	2.34	2.32	~ 2.2
	Calc	2.34	2.47	2.19	2.39

It should be noted that for *Ru*-bpm and *Ru*-dnbpy the characteristic peak around 550 nm is not observed as distinctly as for *Ru*-bpc and *Ru*-bpy. An approximation was made as to the wavelength for the *Ru*-dnbpy absorbance by considering the shoulder starting around 625 nm. However, the spectrum of *Ru*-bpm appears to have no significant absorbance in this region, while calculation would suggest that the characteristic peak should occur around the same wavelength as that of *Ru*-dnbpy. This would suggest that either the excitation around 550 nm is between different molecular orbitals for each of the different catalysts, that less $[Ru^{IV}=O]^{2+}$ is present, or that compound with these ligands is just unstable. Examination of the molecular orbitals involved in the excitation (see Figure S9) shows a similar d – d transition localised on the metal centre for each catalyst (with the unoccupied orbital featuring some delocalisation onto the aromatic ligand). It could therefore be concluded that for the case of *Ru*-bpm and *Ru*-dnbpy, less $[Ru^{IV}=O]^{2+}$ is present after 24 hours.

One might be tempted to attribute this limited presence of $[Ru^{IV}=O]^{2+}$ for *Ru*-bpm and *Ru*-dnbpy to the influence of the different ligand on the oxidation potential of the catalyst, such that the redox potential of CAN would no longer be sufficient to drive the catalyst to this catalytic intermediate. We have therefore computed the energy difference between the first two catalytic steps for all the catalysts examined (see Table 3). These results show that from a thermodynamic point of view there is very little difference among the catalysts, and this cannot explain why *Ru*-bpm and *Ru*-dnbpy show little or no presence of the $[Ru^{IV}=O]^{2+}$ intermediate. Most likely these two derivative catalysts are less stable, and have degraded after 24 hours in the presence of CAN. The lower stability of *Ru*-bpm and *Ru*-dnbpy, and their higher oxidation states in particular, may be explained by referring to literature. Ligands such as 2,2'-bipyrimidine are weaker σ-donors and more effective π-acceptors than 2,2'-bipyridine; they are therefore less able to stabilise upper oxidation states, favouring decomposition through ligand loss.[82]

Table 3. Change in bond energy for the first two catalytic steps for the examined catalysts. The catalytic steps are assumed to work in PCET regime, and thus the energy of the proton and electron is incorporated by using the bond energy of H_2

ΔE (eV)	***Ru*-bpc**	***Ru*-bpy**	***Ru*-mbpy**	***Ru*-dnbpy**	***Ru*-bpm**
ΔE ($[Ru^{III}\text{-}OH]^{2+} + \frac{1}{2}H_2 - [Ru^{II}\text{-}OH_2]^{2+}$)	1.60	1.68	1.57	1.71	1.68
ΔE ($[Ru^{IV}=O]^{2+} + \frac{1}{2}H_2 - [Ru^{III}\text{-}OH]^{2+}$)	1.73	1.63	1.71	1.71	1.73

Pulse radiolysis characterization of $[Ru^{III}\text{-}OH]^{2+}$

Although optical absorption measurements clearly showed the $[Ru^{II}\text{-}OH_2]^{2+}$ and $[Ru^{IV}{=}O]^{2+}$ intermediates, $[Ru^{III}\text{-}OH]^{2+}$, the first PCET intermediate, was not observed. To overcome this problem, pulse radiolysis measurements were made. This technique has two key advantages for tackling these types of problems: it gives access to a wide range of oxidants that can drive the catalyst through its full cycle; and the oxidant can be generated on a time scale of nanoseconds, greatly improving the time resolution.[44] It is therefore a powerful tool for investigating oxidation states that are difficult to access. Here, the derivative catalyst *Ru*-mbpy was used as it reacts with both $SO_4^{\bullet-}$ radicals (produced at neutral and acidic pH) and $CO_3^{\bullet-}$ radicals (produced a basic pH). Experiments were performed in acidic, neutral and basic conditions. However, in neutral and basic conditions, the spectra of the transient oxidized species were not observed, most likely as their lifetime at pH > 3 is below the instrumental resolution (< 10 ns). But the oxidizing $CO_3^{\bullet-}$ (Figure S11) or $SO_4^{\bullet-}$ radical did disappear, thereby showing their reactivity with the complex.

The transient spectra of the first PCET intermediate observed at acidic pH are shown in Figure 7 (similar spectra obtained with a dose per pulse = 80 Gy are shown in Figure S12). A strong band between 300 and 400 nm can clearly be seen. This band is ascribed to ligand-centred π-π* transitions. Two less intense peaks are observed: at 480 and, much weaker, at 600 nm. The latter can be assigned to LMCT transitions, from π (bipyridyl) to partially filled dπ (e_g) orbitals of the Ru^{III} centre, as confirmed by DFT calculations (see Figure S13).[77] On the other hand, the absorption bands in the range between 300 and 550 nm can be attributed to MLCT transitions (from dπ (t_{2g}) orbitals of the Ru^{III} to π (bpy) orbitals), in agreement with the literature.[77,83,84]

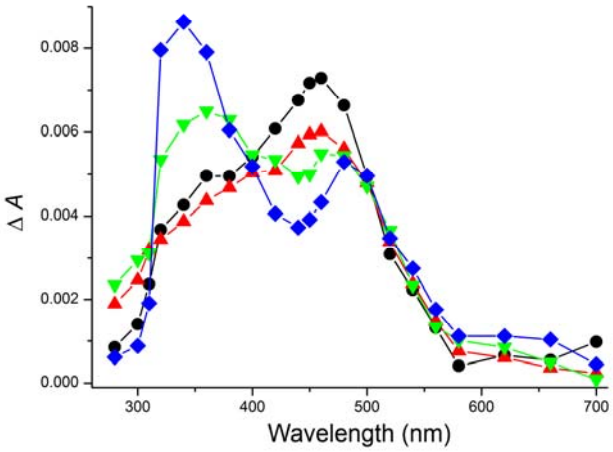

Figure 7. Transient absorption spectra obtained by $SO_4^{\bullet-}$ radical oxidation of *Ru*-mbpy (c = 10^{-5} M) after pulse radiolysis of Argon purged solution containing 10 mM $K_2S_2O_8$ and 0.1 M *t*-BuOH at pH = 1.4. The different curves represent the absorption spectra detected at 1.5 µs (black), 3 µs (red), 5 µs (green), and 15-40 µs (blue) after the pulse. Optical path = 2 cm, dose per pulse = 37.7 Gy.

By increasing $K_2S_2O_8$ concentration up to 0.15 M and decreasing *Ru*-mbpy concentration to 7 µM at pH = 1.4, it was possible to follow the decay of $SO_4^{\bullet-}$ as a function of [*Ru*-mbpy]. Under these conditions all the hydrated electrons are captured by $S_2O_8^{2-}$. The spectra, reported in Figure S14, show only the typical band of $SO_4^{\bullet-}$. From this experiment it was possible to obtain the value of $k(SO_4^{\bullet-} + Ru\text{-mbpy}) = (3.6 \pm 0.3) \times 10^9\ M^{-1}\ s^{-1}$.

TDDFT calculations of $[Ru^{III}\text{-}OH]^{2+}$

The spectra for the $[Ru^{III}\text{-}OH]^{2+}$ intermediates were calculated for each catalyst as shown in Figure 8.

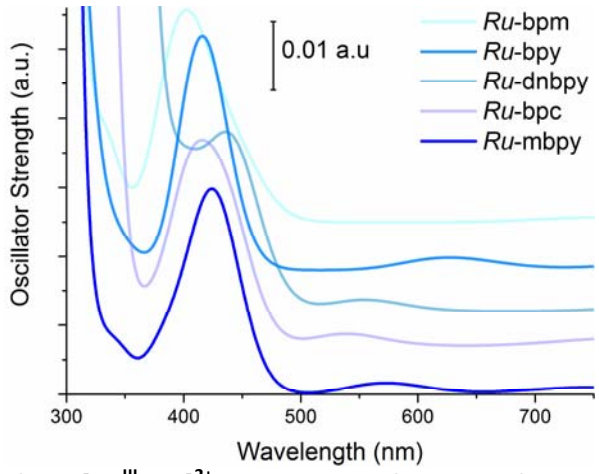

Figure 8. TDDFT spectra of the $[Ru^{III}\text{-}OH]^{2+}$ intermediate for each of the catalysts examined in this work. The curves have a Gaussian width broadening of 0.3 eV and have, for clarity, been offset in the Y direction.

All catalysts show a primary excitation around 420 nm, while a less intense peak is observed between 550 – 625 nm. This secondary peak is due to a LMCT transition (see Figure S9). The differing excitation wavelengths are expected because the ligands differ, and thus also the energy of the orbital localised on the ligand. In the case of *Ru*-bpm this excitation occurs at sufficiently high energies such that it appears as a slight shoulder of the primary excitation (see also Table S5). We can conclude that the difference in the wavelength between these two peaks is characteristic for each catalyst. By comparing the calculated TDDFT spectrum of *Ru*-mbpy to the pulse radiolysis spectra (Table 4), it can be seen that the difference in the position of the two peaks agrees reasonably well, even though the absolute position of the peaks is significantly shifted to lower energy in the computed spectrum. This is likely due to the environmental effects within the pulse radiolysis experiments, which are not included theoretically. This analysis supports the observation of the $[Ru^{III}\text{-}OH]^{2+}$ intermediate.

Table 4. The two primary excitations for the $[Ru^{III}\text{-}OH]^{2+}$ intermediate calculated using TDDFT (Calc), as compared to the two peaks observed in pulse radiolysis measurements of *Ru*-mbpy (Exp). Values are reported both in nm and in eV. In the last column we report the difference in the position of the two peaks.

		λ_1	λ_2	λ_2-λ_1
Wavelength (nm)	Exp	480	~ 620	140
	Calc	424	573	149
		E_1	E_2	E_1-E_2
Energy (eV)	Exp	2.6	2.0	0.6
	Calc	2.92	2.16	0.76

Recently there have been a number of, initially monomeric, iridium based water oxidation catalysts which have been shown to form a dimeric active species. [32,67] An initial exploration was performed as to the possibility of dimer formation using a number of possible dimers (the computationally stable ones are shown in the Supplementary Information). However, preliminary calculations do not provide clear evidence of dimer formation. A more in-depth investigation may be performed, but falls outside the scope of this work.

Conclusions

A group of mononuclear ruthenium water oxidation catalysts has been analysed with the main goal of characterizing their catalytic mechanism. Catalyst stability is established using OLEMS and SERS. Electrochemical data combined with free-energy calculations using density functional theory clearly point to a catalytic cycle involving four consecutive proton-coupled electron transfer steps. The most thermodynamic demanding step is the third PCET step starting from the Ru-oxo species and involving the oxygen-oxygen bond formation, which shows an overpotential of about 0.6 V for all the complexes studied. The comparisons between the experimental optical properties and the absorption spectra computed with time-dependent DFT, as well as between SERS and Raman frequency calculations, provide a convincing validation of the proposed catalytic cycle and a clear characterization of the intermediate complexes observed spectroscopically. This combination of experimental data with DFT based modelling is indeed an ideal strategy that can be generally applied in the characterisation of water oxidation catalysts.

Acknowledgements

The use of supercomputer facilities was sponsored by NWO Physical Sciences, with financial support from the Netherlands Organization for Scientific Research (NWO). K.S.J. acknowledges the Higher Education Commission (HEC), Pakistan, for the research grant. This research is also financed by the NWO-ECHO project number 713.011.002, by the BioSolar Cells open innovation consortium, supported by the Dutch Ministry of Economic Affairs, Agriculture and Innovation (project C1.9) and by the Italian National Research Council (CNR, "SolarFuelTandem") within the EUROCORES Programme EuroSolarFuels of the European Science Foundation (ESF). A.B. thanks the CNR project PM.P04.010 (MACOL) and the "Progetto Bandiera" N-CHEM.

ASSOCIATED CONTENT

Supporting Information (SI): Synthesis methods of the starting compounds $[Ru^{II}(cy)(L)(Cl)]Cl$; validation of the TDDFT methodology used; UV-Vis absorption data for the $[Ru(cy)(L)(H_2O)]^{2+}$ complexes; the calculated absorption spectra for each proposed intermediate in the catalytic cycle of *Ru*-bpy, as well as molecular orbitals involved in relevant excitations; the cyclic voltammogram of *Ru*-bpc and *Ru*-bpy; additional information used in the elucidation of $[Ru^{III}\text{-}OH]^{2+}$ including the energies of, and molecular orbitals involved in, the primary excitations, as well as details for pulse radiolysis in basic and acidic solutions. This material is available free of charge via the Internet at http://pubs.acs.org.

AUTHOR INFORMATION

Corresponding Author

*Email: f.buda@chem.leidenuniv.nl

Notes

The authors declare no competing financial interests.

References

(1) Thapper, A.; Styring, S.; Saracco, G.; Rutherford, A. W.; Robert, B.; Magnuson, A.; Lubitz, W.; Llobet, A.; Kurz, P.; Holzwarth, A.; Fiechter, S.; de Groot, H.; Campagna, S.; Braun, A.; Bercegol, H.; Artero, V. *Green* **2013**, *3*, 43–57.

(2) Young, K. J.; Martini, L. A.; Milot, R. L.; Snoeberger III, R. C.; Batista, V. S.; Schmuttenmaer, C. A.; Crabtree, R. H.; Brudvig, G. W. *Coord. Chem. Rev.* **2012**, *256*, 2503–2520.

(3) Gust, D.; Moore, T. A.; Moore, A. L. *Acc. Chem. Res.* **2009**, *42*, 1890–1898.

(4) Duan, L.; Bozoglian, F.; Mandal, S.; Stewart, B.; Privalov, T.; Llobet, A.; Sun, L. *Nat. Chem.* **2012**, *4*, 418–423.

(5) Duan, L.; Araujo, C. M.; Ahlquist, M. S. G.; Sun, L. *Proc. Natl. Acad. Sci.* **2012**, *109*, 15584–15588.

(6) Duan, L.; Xu, Y.; Gorlov, M.; Tong, L.; Andersson, S.; Sun, L. *Chem. – Eur. J.* **2010**, *16*, 4659–4668.

(7) Tong, L.; Duan, L.; Xu, Y.; Privalov, T.; Sun, L. *Angew. Chem. Int. Ed.* **2011**, *50*, 445–449.

(8) Hetterscheid, D. G. H.; Reek, J. N. H. *Angew. Chem. Int. Ed.* **2012**, *51*, 9740–9747.

(9) Kaveevivitchai, N.; Zong, R.; Tseng, H.-W.; Chitta, R.; Thummel, R. P. *Inorg. Chem.* **2012**, *51*, 2930–2939.

(10) Barnett, S. M.; Goldberg, K. I.; Mayer, J. M. *Nat. Chem.* **2012**, *4*, 498–502.

(11) Blakemore, J. D.; Schley, N. D.; Balcells, D.; Hull, J. F.; Olack, G. W.; Incarvito, C. D.; Eisenstein, O.; Brudvig, G. W.; Crabtree, R. H. *J. Am. Chem. Soc.* **2010**, *132*, 16017–16029.

(12) Wasylenko, D. J.; Palmer, R. D.; Berlinguette, C. P. *Chem. Commun.* **2013**, *49*, 218.

(13) Polyansky, D. E.; Muckerman, J. T.; Rochford, J.; Zong, R.; Thummel, R. P.; Fujita, E. *J. Am. Chem. Soc.* **2011**, *133*, 14649–14665.

(14) Savini, A.; Bellachioma, G.; Ciancaleoni, G.; Zuccaccia, C.; Zuccaccia, D.; Macchioni, A. *Chem. Commun.* **2010**, *46*, 9218–9219.

(15) Dau, H.; Limberg, C.; Reier, T.; Risch, M.; Roggan, S.; Strasser, P. *ChemCatChem* **2010**, *2*, 724–761.

(16) Natali, M.; Berardi, S.; Sartorel, A.; Bonchio, M.; Campagna, S.; Scandola, F. *Chem. Commun.* **2012**, *48*, 8808–8810.

(17) Stewart, D. J.; Concepcion, J. J.; Brennaman, M. K.; Binstead, R. A.; Meyer, T. J. *Proc. Natl. Acad. Sci.* **2013**, *110*, 876–880.

(18) Wang, T.; Brudvig, G. W.; Batista, V. S. *J. Chem. Theory Comput.* **2010**, *6*, 2395–2401.

(19) Lv, H.; Geletii, Y. V.; Zhao, C.; Vickers, J. W.; Zhu, G.; Luo, Z.; Song, J.; Lian, T.; Musaev, D. G.; Hill, C. L. *Chem. Soc. Rev.* **2012**, *41*, 7572–7589.

(20) Zeng, Q.; Lewis, F. W.; Harwood, L. M.; Hartl, F. *Coord. Chem. Rev.* **2015**, *304–305*, 88–101.

(21) Vallés-Pardo, J. L.; Guijt, M. C.; Iannuzzi, M.; Joya, K. S.; de Groot, H. J. M.; Buda, F. *ChemPhysChem* **2012**, *13*, 140–146.

(22) Kärkäs, M. D.; Åkermark, T.; Johnston, E. V.; Karim, S. R.; Laine, T. M.; Lee, B.-L.; Åkermark, T.; Privalov, T.; Åkermark, B. *Angew. Chem. Int. Ed.* **2012**, *51*, 11589–11593.

(23) Marelius, D. C.; Bhagan, S.; Charboneau, D. J.; Schroeder, K. M.; Kamdar, J. M.; McGettigan, A. R.; Freeman, B. J.; Moore, C. E.; Rheingold, A. L.; Cooksy, A. L.; Smith, D. K.; Paul, J. J.; Papish, E. T.; Grotjahn, D. B. *Eur. J. Inorg. Chem.* **2014**, *2014*, 676–689.

(24) Hetterscheid, D. G. H.; Reek, J. N. H. *Chem. Commun.* **2011**, *47*, 2712–2714.

(25) Joya, K. S.; Subbaiyan, N. K.; D'Souza, F.; de Groot, H. J. M. *Angew. Chem. Int. Ed.* **2012**, *51*, 9601–9605.

(26) Blakemore, J. D.; Schley, N. D.; Olack, G. W.; Incarvito, C. D.; Brudvig, G. W.; Crabtree, R. H. *Chem. Sci.* **2010**, *2*, 94–98.

(27) Lalrempuia, R.; McDaniel, N. D.; Müller-Bunz, H.; Bernhard, S.; Albrecht, M. *Angew. Chem. Int. Ed.* **2010**, *49*, 9765–9768.

(28) Vagnini, M. T.; Smeigh, A. L.; Blakemore, J. D.; Eaton, S. W.; Schley, N. D.; D'Souza, F.; Crabtree, R. H.; Brudvig, G. W.; Co, D. T.; Wasielewski, M. R. *Proc. Natl. Acad. Sci.* **2012**, *109*, 15651–15656.
(29) Hull, J. F.; Balcells, D.; Blakemore, J. D.; Incarvito, C. D.; Eisenstein, O.; Brudvig, G. W.; Crabtree, R. H. *J. Am. Chem. Soc.* **2009**, *131*, 8730–8731.
(30) de Respinis, M.; Joya, K. S.; De Groot, H. J. M.; D'Souza, F.; Smith, W. A.; van de Krol, R.; Dam, B. *J. Phys. Chem. C* **2015**.
(31) Joya, K. S.; de Groot, H. J. M. *Int. J. Hydrog. Energy* **2012**, *37*, 8787–8799.
(32) Diaz-Morales, O.; Hersbach, T. J. P.; Hetterscheid, D. G. H.; Reek, J. N. H.; Koper, M. T. M. *J. Am. Chem. Soc.* **2014**, *136*, 10432–10439.
(33) Wonders, A. H.; Housmans, T. H. M.; Rosca, V.; Koper, M. T. M. *J. Appl. Electrochem.* **2006**, *36*, 1215–1221.
(34) Diaz-Morales, O.; Calle-Vallejo, F.; Munck, C. de; Koper, M. T. M. *Chem. Sci.* **2013**, *4*, 2334–2343.
(35) Lai, S. C. S.; Kleyn, S. E. F.; Rosca, V.; Koper, M. T. M. *J. Phys. Chem. C* **2008**, *112*, 19080–19087.
(36) Gao, P.; Gosztola, D.; Leung, L.-W. H.; Weaver, M. J. *J. Electroanal. Chem. Interfacial Electrochem.* **1987**, *233*, 211–222.
(37) Suntivich, J.; Gasteiger, H. A.; Yabuuchi, N.; Shao-Horn, Y. *J. Electrochem. Soc.* **2010**, *157*, B1263–B1268.
(38) Buxton, G. V.; Mulazzani, Q. G. In *Electron Transfer in Chemistry*; Wiley-VCH Verlag GmbH, 2001; pp 503–557.
(39) Hutton, A.; Roffi, G.; Martelli, A. *Quad Area Ric Emilia-Romagna* **1974**, *5*, 67.
(40) Mulazzani, Q. G.; D'Angelantonio, M.; Venturi, M.; Hoffman, M. Z.; Rodgers, M. A. J. *J. Phys. Chem.* **1986**, *90*, 5347–5352.
(41) Buxton, G. V.; Greenstock, C. L.; Helman, W. P.; Ross, A. B. *J. Phys. Chem. Ref. Data* **1988**, *17*, 513–886.
(42) Wardman, P. *J. Phys. Chem. Ref. Data* **1989**, *18*, 1637–1755.
(43) Wadsworth, E.; Duke, F. R.; Goetz, C. A. *Anal. Chem.* **1957**, *29*, 1824–1825.
(44) Polyansky, D. E.; Hurst, J. K.; Lymar, S. V. *Eur. J. Inorg. Chem.* **2014**, *2014*, 619–634.
(45) Guerra, C. F.; Snijders, J. G.; Velde, G. te; Baerends, E. J. *Theor. Chem. Acc.* **1998**, *99*, 391–403.
(46) te Velde, G.; Bickelhaupt, F. M.; Baerends, E. J.; Fonseca Guerra, C.; van Gisbergen, S. J. A.; Snijders, J. G.; Ziegler, T. *J. Comput. Chem.* **2001**, *22*, 931–967.
(47) SCM. *ADF 2012*; Theoretical Chemistry, Vrije Universiteit, Amsterdam, The Netherlands.
(48) Grimme, S.; Ehrlich, S.; Goerigk, L. *J. Comput. Chem.* **2011**, *32*, 1456–1465.
(49) Swart, M.; Ehlers, A. W.; Lammertsma, K. *Mol. Phys.* **2004**, *102*, 2467–2474.
(50) Groenhof, A. R.; Ehlers, A. W.; Lammertsma, K. *J. Am. Chem. Soc.* **2007**, *129*, 6204–6209.
(51) Liao, M.-S.; Watts, J. D.; Huang, M.-J. *J. Phys. Chem. A* **2007**, *111*, 5927–5935.
(52) Güell, M.; Luis, J. M.; Siegbahn, P. E. M.; Solà, M. *JBIC J. Biol. Inorg. Chem.* **2009**, *14*, 273–285.
(53) Stephens, P. J.; Devlin, F. J.; Chabalowski, C. F.; Frisch, M. J. *J. Phys. Chem.* **1994**, *98*, 11623–11627.
(54) Klamt, A. *COSMO-RS: From Quantum Chemistry to Fluid PhaseThermodynamics and Drug Design*; Elsevier Science: Amsterdam, 2005.
(55) Nørskov, J. K.; Rossmeisl, J.; Logadottir, A.; Lindqvist, L.; Kitchin, J. R.; Bligaard, T.; Jónsson, H. *J. Phys. Chem. B* **2004**, *108*, 17886–17892.
(56) Rossmeisl, J.; Logadottir, A.; Nørskov, J. K. *Chem. Phys.* **2005**, *319*, 178–184.
(57) Rossmeisl, J.; Qu, Z.-W.; Zhu, H.; Kroes, G.-J.; Nørskov, J. K. *J. Electroanal. Chem.* **2007**, *607*, 83–89.
(58) M. J. Frisch; G. W. Trucks; H. B. Schlegel; G. E. Scuseria. *Gaussian 09, Revision D.01*; Gaussian, Inc.,Wallingford CT, 2009.
(59) Wadt, W. R.; Hay, P. J. *J. Chem. Phys.* **1985**, *82*, 284–298.

(60) Hay, P. J.; Wadt, W. R. *J. Chem. Phys.* **1985**, *82*, 299–310.
(61) Hay, P. J.; Wadt, W. R. *J. Chem. Phys.* **1985**, *82*, 270–283.
(62) Chandrasekharam, M.; Kumar, C. P.; Singh, S. P.; Anusha, V.; Bhanuprakash, K.; Islam, A.; Han, L. *RSC Adv.* **2013**, *3*, 26035–26046.
(63) Rodríguez, S.; Qu, B.; Fandrick, K. R.; Buono, F.; Haddad, N.; Xu, Y.; Herbage, M. A.; Zeng, X.; Ma, S.; Grinberg, N.; Lee, H.; Han, Z. S.; Yee, N. K.; Senanayake, C. H. *Adv. Synth. Catal.* **2014**, *356*, 301–307.
(64) Tomasi, J.; Mennucci, B.; Cammi, R. *Chem. Rev.* **2005**, *105*, 2999–3094.
(65) O'Boyle, N. M.; Tenderholt, A. L.; Langner, K. M. *J. Comput. Chem.* **2008**, *29*, 839–845.
(66) Savini, A.; Belanzoni, P.; Bellachioma, G.; Zuccaccia, C.; Zuccaccia, D.; Macchioni, A. *Green Chem.* **2011**, *13*, 3360–3374.
(67) Hintermair, U.; Sheehan, S. W.; Parent, A. R.; Ess, D. H.; Richens, D. T.; Vaccaro, P. H.; Brudvig, G. W.; Crabtree, R. H. *J. Am. Chem. Soc.* **2013**, *135*, 10837–10851.
(68) Yamada, H.; Hurst, J. K. *J. Am. Chem. Soc.* **2000**, *122*, 5303–5311.
(69) DePasquale, J.; Nieto, I.; Reuther, L. E.; Herbst-Gervasoni, C. J.; Paul, J. J.; Mochalin, V.; Zeller, M.; Thomas, C. M.; Addison, A. W.; Papish, E. T. *Inorg. Chem.* **2013**, *52*, 9175–9183.
(70) Wasylenko, D. J.; Ganesamoorthy, C.; Henderson, M. A.; Berlinguette, C. P. *Inorg. Chem.* **2011**, *50*, 3662–3672.
(71) Parent, A. R.; Crabtree, R. H.; Brudvig, G. W. *Chem. Soc. Rev.* **2013**, *42*, 2247–2252.
(72) Moonshiram, D.; Purohit, V.; Concepcion, J. J.; Meyer, T. J.; Pushkar, Y. *Materials* **2013**, *6*, 392–409.
(73) Badiei, Y. M.; Polyansky, D. E.; Muckerman, J. T.; Szalda, D. J.; Haberdar, R.; Zong, R.; Thummel, R. P.; Fujita, E. *Inorg. Chem.* **2013**, *52*, 8845–8850.
(74) Staehle, R.; Tong, L.; Wang, L.; Duan, L.; Fischer, A.; Ahlquist, M. S. G.; Sun, L.; Rau, S. *Inorg. Chem.* **2014**, *53*, 1307–1319.
(75) Wasylenko, D. J.; Ganesamoorthy, C.; Koivisto, B. D.; Henderson, M. A.; Berlinguette, C. P. *Inorg. Chem.* **2010**, *49*, 2202–2209.
(76) Wang, L.; Duan, L.; Wang, Y.; Ahlquist, M. S. G.; Sun, L. *Chem. Commun.* **2014**, *50*, 12947–12950.
(77) Concepcion, J. J.; Tsai, M.-K.; Muckerman, J. T.; Meyer, T. J. *J. Am. Chem. Soc.* **2010**, *132*, 1545–1557.
(78) Kottrup, K. G.; Hetterscheid, D. G. H. *Chem. Commun.* **2016**, *52*, 2643–2646.
(79) Vallés Pardo, J. L. In silico study of reaction mechanisms and design principles for water oxidation catalysts. Dissertatie, Universiteit Leiden: Leiden, 2012.
(80) Paeng, I. R.; Nakamoto, K. *J. Am. Chem. Soc.* **1990**, *112*, 3289–3297.
(81) Freedman, D. A.; Kruger, S.; Roosa, C.; Wymer, C. *Inorg. Chem.* **2006**, *45*, 9558–9568.
(82) Allen, G. H.; White, R. P.; Rillema, D. P.; Meyer, T. J. *J. Am. Chem. Soc.* **1984**, *106*, 2613–2620.
(83) Hohloch, S.; Schweinfurth, D.; Sommer, M. G.; Weisser, F.; Deibel, N.; Ehret, F.; Sarkar, B. *Dalton Trans.* **2014**, *43*, 4437–4450.
(84) Nazeeruddin, M. K.; Zakeeruddin, S. M.; Kalyanasundaram, K. *J. Phys. Chem.* **1993**, *97*, 9607–9612.

TABLE OF CONTENTS GRAPHICS